Ceria in an oxygen environment: Surface phase equilibria and its descriptors

Venkatesh Botu [a,b], Rampi Ramprasad [a,c], Ashish B. Mhadeshwar [a,b],*

[a] Department of Chemical, Materials, and Biomolecular Engineering, University of Connecticut, Storrs, CT 06269, United States
[b] Center for Clean Energy Engineering, University of Connecticut, Storrs, CT, United States
[c] Institute of Materials Science, University of Connecticut, Storrs, CT 06269, United States

ABSTRACT

Ceria offers great promise in catalysis, due to its facile switchable oxidation state manifested from its oxygen buffering capability. This work presents the first equilibrium surface phase diagram of ceria exposed to various oxygen providing reservoirs (e.g., a pure O_2 reservoir as well as NO/NO_2, H_2/H_2O, or CO/CO_2 redox environments) using first principles thermodynamics. For a pure O_2 environment, the stoichiometric ceria (111) surface is favored at ambient conditions. Any appreciable surface reduction is observed only at ultra-low oxygen partial pressures ($<10^{-30}$ atm) and room temperature or at temperatures >2000 K and ambient pressures. On the other hand, a redox environment promotes surface reduction at temperatures as low as 300 K. Semi-local, Hubbard modified semi-local, and hybrid electronic exchange-correlation functionals are used to capture the energetics and phase transitions. We observe no difference between the three theories in the energetics governing ceria surface reduction in the dilute limit. The predicted phase transitions by all levels of theory are in agreement with each other and in excellent agreement with literature experimental data. Creation of oxygen vacancies in the sub-surface is energetically favored over surface vacancies, and is pivotal in determining the key features of the surface phase diagram. Consequently, we identify the oxygen vacancy formation energy as a descriptor for the surface reactivity of ceria in various oxygen environments. This single governing factor could be used in future studies to probe the surface reactivity of ceria and also to design improved ceria-based materials for redox reactions.

© 2013 Elsevier B.V. All rights reserved.

1. Introduction

Oxides of cerium (CeO_2 and Ce_2O_3) possess a peculiar characteristic of being able to regulate their oxygen content based on the operating environment. This "buffering" capability makes them suitable for redox reactions, e.g., during the treatment of automotive emissions in fuel-rich or -lean environments. More recently, this functional merit of cerium oxides has been harnessed in solid oxide fuel cell electrolytes to regulate oxygen transfer between the cathode and anode compartments [1]. Another application of cerium oxides is in high temperature gas sensors and thermochemical water splitters that rely on alternating oxidized and reduced states of cerium oxides [2,3]. Finally, a prominent application of cerium oxides is in catalysis, particularly for the water–gas shift (WGS) reaction ($CO + H_2O \rightarrow CO_2 + H_2$). Recent studies indicate that the oxide support actively participates in the reaction, in addition to providing structural integrity to the metal catalyst [4–7]. A governing factor in all these applications is the role of oxygen within the ceria lattice or at the surface. Therefore, developing a fundamental understanding of the

oxygen interaction with ceria is of paramount importance in discerning the chemical properties of cerium oxides in various oxygen environments. Knowing the surface/lattice chemistry allows one to rapidly tailor materials based on desired characteristics (e.g., reactivity, selectivity, and stability, to name a few).

Regulating the O stoichiometry in ceria offers a promising prospect in catalysis given the existence of multivalent cationic states. In reactions involving a net transfer of O such as WGS, ceria is believed to play an intermediary role of providing redox sites for the reactants [8,9]. The current understanding of the reaction mechanisms involving ceria is based upon experimental results and first principles calculations. Ample experimental data characterizing O non-stoichiometry of ceria exists, primarily from a few decades ago. In the 1980's, Bevan and Kordis equilibrated ceria in a mixture of either H_2O/H_2 or CO_2/CO and measured the partial pressures of the corresponding gases to determine the oxygen non-stoichiometry at 10^{-8}–10^{-32} atm and 909–1443 K [10]. Panlener et al. performed similar non-stoichiometry studies using thermo-gravimetric measurements over 1023–1773 K and 10^{-2}–10^{-26} atm oxygen partial pressure [11]. Additional experiments (mass spectrometry, effusion measurements, high temperature X-ray diffraction, thermal expansion measurements, and specific heat measurements) studying the non-stoichiometry of ceria, along with those discussed above, indicate that

high temperatures and low oxygen partial pressures are required to observe any appreciable reduction of the undoped bulk CeO_2 or any appreciable changes in its equilibrium fluorite crystal structure (Fig. 1a) [12–15]. Within the context of catalysis, non-stoichiometry at the ceria surface introduced by point defects such as O vacancies is crucial for the creation of active reaction sites. These vacancies can be formed either in the surface or sub-surface O layer (Fig. 1b), as elaborated in the work by Torbrugge and Reichling [16]. Using atomic and dynamic force microscopy, they revealed that the preferred position of the O vacancies is the sub-surface region for ceria annealed at ~1200 K and 10^{-12} atm.

The availability of such experimental information on the stoichiometry of ceria and the importance of vacancies in processes involving ceria have provided the motivation and testing ground for parallel and complementary first principles computational studies. While extensive first principles density functional theory (DFT) studies exist for bulk ceria, there is a limited understanding on the transitions between stoichiometric and non-stoichiometric surface phases. Past computational studies on ceria have led to a deeper understanding of its electronic and structural properties, stable surface orientation, and the role of oxygen diffusion and vacancies within the bulk lattice [17–27]. These include identification of the O vacancy as a crucial factor in determining the activity of ceria in chemical reactions [28,29]. It is suggested that O vacancies are preferably formed in the sub-surface layer rather than the surface layer (or within the bulk) [30], which is consistent with the aforementioned experiments. Recent work by Janik and colleagues further indicates the significance of O vacancies in activating a ceria surface for hydrocarbon conversion [31]. Vacancies reduce the neighboring Ce atoms making them active for dissociation of gas phase molecules. Fronzi et al. studied the surface behavior of ceria in the presence of a water and oxygen environment [32]. They found that water remains adsorbed on the surface even under extremely low water partial pressures (~10^{-10} atm), at a temperature of 300 K and oxygen pressure of 1 atm. Under these conditions, reduction in the oxygen pressure induces O vacancies and water dissociation into OH and H. Thus, O vacancies increase the surface reactivity of ceria for water dissociation.

Even though significant work has been conducted on ceria using first principles calculations, ceria still poses technical difficulties due to localization of electrons in the 4f orbitals leading to increased columbic repulsion as it undergoes reduction. These effects are not captured by conventional DFT that uses local or semi-local electronic exchange-correlation functionals [28,33,34]. The general practice of modeling cerium oxides has evolved from the traditional functionals to functionals modified using the Hubbard parameter (U) [35,36] and to hybrid functionals [17]. Furthermore, while most of the zero-temperature DFT studies [17,19–25,31] have provided substantial understanding of the

role of oxygen chemistry, a more quantitative connection with the available experimental data for ceria stoichiometry requires a treatment that includes non-zero temperatures and pressures. First principles thermodynamics (FPT) combines zero-temperature DFT results with statistical thermodynamics concepts, and offers a reliable, practical, and powerful prescription to address such factors [37–39].

In the present contribution, we have considered several ceria surface non-stoichiometric configurations and used DFT–FPT to determine the favored surface stoichiometry of ceria in equilibrium with a given oxygen environment over a wide range of temperatures and pressures. Fig. 2, for instance, shows the essence of our current findings, in which such an equilibrium surface phase diagram of ceria exposed to a pure O_2 environment is portrayed, along with available experimental data to highlight the level of fidelity that can be achieved in such DFT–FPT studies. The surface phase diagrams shown in Fig. 2 are determined at three levels of theory: the first one (panel a) using a conventional semi-local electron exchange-correlation functional, the second one (panel b) using the Hubbard modified exchange-correlation functional accounting for increased electronic repulsion, and the third one (panel c) utilizing a hybrid functional incorporating a certain amount of screened nonlocal exchange interaction. Phase diagrams corresponding to other chemical environments that can provide an indirect oxygen source (e.g., NO/NO_2, H_2/H_2O, and CO/CO_2) are also determined in this work, and their features compare favorably with the available experimental data (discussed later).

The key findings from this work are as follows: (i) A redox environment promotes surface reduction compared to a pure O_2 reservoir. (ii) The computationally expensive hybrid or Hubbard modified functionals show a marginal difference compared to the semi-local exchange-correlation functionals. (iii) The sub-surface O vacancy formation energy is the single most important factor in determining significant features of the ceria surface diagram in an O_2 or redox environment. The last finding has deeper implications for future attempts aimed at methods to control features of the surface phase diagram; and we thus elaborate on that point further. Equilibrium phase diagrams, by definition, do not contain any kinetic information. Nevertheless, key phase boundaries in the phase diagrams may be indicative of catalytically active conditions, as elucidated in the past for CO oxidation over RuO_2 and Pd surfaces by Scheffler and colleagues [37–39]. Consistent with the Sabatier principle, such studies have established that experimentally observed catalytically active regions occur primarily when surface phases undergo transition. Similarly, for a stoichiometric CeO_2 surface, the conditions corresponding to the formation of a subsurface O vacancy indicate the point at which the Ce oxidation state begins to become "flexible", and may be an important factor to track. The O vacancy formation energy in various chemical
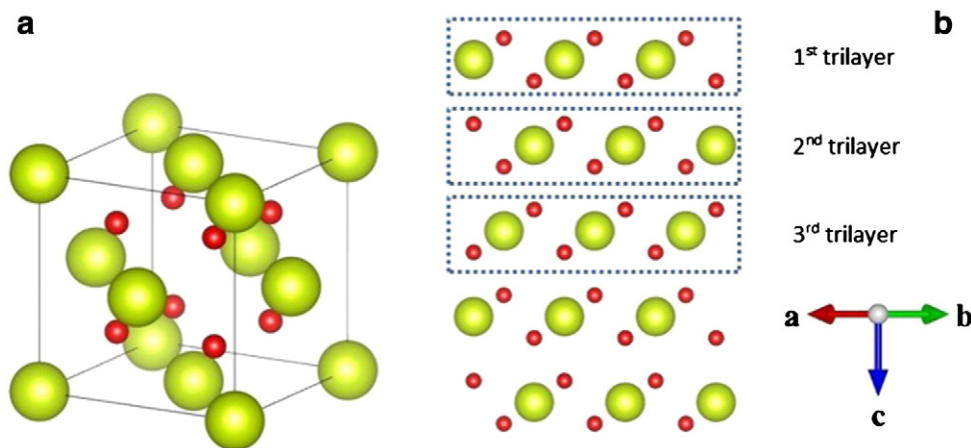

Fig. 1. (a) Fluorite structure of ceria and (b) a 5-trilayer slab model of the ceria (111) surface. Green atoms represent Ce and red atoms represent O. The box represents one trilayer consisting of Ce and the top and bottom O atomic layers. The a, b, and c axes of the surface model are shown at the bottom right corner.
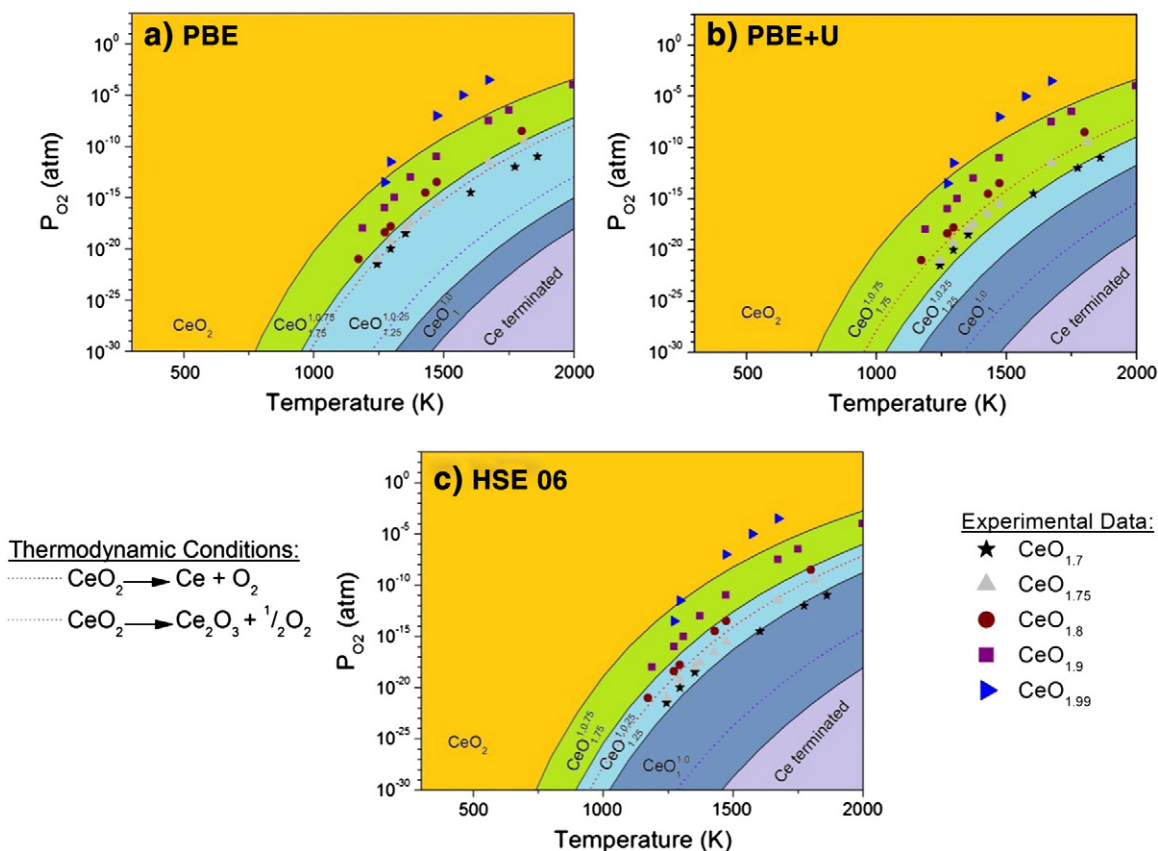
Fig. 2. Predicted ceria surface phase diagram in an oxygen environment using the (a) PBE, (b) PBE + U, and (c) HSE06 levels of theory. Symbols represent experimental data [10,11], and the dashed lines indicate thermodynamically governed relations based on PBE.

environments may thus be viewed as a *descriptor* for catalyst screening studies in the future.

The remainder of this manuscript is organized as follows. In Section 2, we discuss our methodology for the DFT calculations and the FPT framework. Our main results are presented in Section 3, which starts with the 0 K O adatom(s) binding and O vacancy formation energies, followed by the surface energies for different O vacancy concentrations (surface and sub-surface) and the relative surface energies of all configurations as a function of oxygen chemical potential. The penultimate part of this section presents the first principles derived surface phase diagram for ceria in an oxidizing environment based on equilibrium with oxygen, along with a Bader analysis to rationalize the oxidation states of the stable phases. We end this section with the surface phase diagrams in different environments in which the oxygen chemical potential is defined in terms of redox reactions involving NO/NO_2, H_2/H_2O, or CO/CO_2 and the implications of this work. Lastly, we conclude with key points of the current study in Section 4.

2. Methodology

2.1. Computational and model details

All first principles DFT calculations were performed using the plane-wave based Vienna Ab-Initio Simulation Package (VASP) [40]. Projector augmented wave (PAW) frozen core potentials with the O 2s, 2p, and the Ce 5s, 5p, 4f, 5d, 6s states treated as the valence states were employed [41,42]. A 400 eV plane-wave cut-off energy was necessary to ensure converged results. The quantum mechanical part of the electron–electron interactions was represented using the Perdew–Burke–Ernzerhof (PBE) exchange-correlation functional, and its Hubbard modified extension (PBE + U, $U = 5$ eV) along with the Heyd–

Scuseria–Ernzerhof (HSE06) hybrid functional [43–46]. While the PBE functional is a widely used semi-local functional, the HSE06 functional incorporates a certain amount of screened range-separated nonlocal exchange interaction, known to improve various properties including thermochemistry (i.e., energetics) and the electronic structure (e.g., the band gap of insulators) [17]. The Hubbard modified PBE functional, on the other hand, accounts for the increased Coulombic repulsion due to electron localization on a reduced surface. As the HSE06 functional requires significantly more computational time relative to the PBE functional, all geometry optimization calculations were performed using the PBE functional, followed by the evaluation of just the energies using the HSE06 functional at the PBE-optimized geometry. For completeness, geometry and electronic optimization was carried out with PBE + U functional; and it was included here primarily to compare and contrast the three levels of theory. A convergence criterion of 10^{-4} eV and 10^{-3} eV between consecutive electronic and ionic iterations was adopted. A 0.1 eV Gaussian smearing width was used to treat the band occupancies close to the Fermi level. Spin polarized calculations assured correct treatment of the magnetic components of the ceria system, particularly in treating the atomic O, molecular O_2, and reduced Ce atom states.

The bulk ceria fluorite structure in Fig. 1a was optimized using a gamma centered $6 \times 6 \times 6$ k-point mesh and the PBE functional, yielding a lattice parameter of 5.47 Å, which is reasonably close to the experimental value of 5.41 Å [47]. Similarly optimization based on PBE + U functional resulted in a lattice parameter of 5.49 Å for the bulk structure. Using the PBE optimized bulk lattice parameters, a 2×2 ceria slab was created to model the (111) surface with a total of 15 atomic layers (Fig. 1b) and a vacuum of 15 Å between periodic images to minimize the finite size interactions. As shown in Fig. 1b, stacking along the

(111) direction can be represented in terms of [O–Ce–O] trilayers, with equal number of atoms in each layer of a trilayer for a stoichiometric CeO_2 system. Therefore, the 15 atomic layers consist of 5 such trilayers. For the 1st trilayer, we refer to the upper and lower O layers as the surface and sub-surface layers, respectively. The k-point grid was reduced to $3 \times 3 \times 1$ for the slab supercell, and the middle 3 trilayers were fixed to create a bulk-like region, yielding a symmetric surface model. Fig. 3 shows the top and the side views of the supercell used to model the crystal surface (only the top two trilayers of the surface are shown for clarity). The green and gray spheres represent Ce atoms in the first and second trilayers, respectively. The red, black, and blue atoms represent the surface, sub-surface, and adsorbed (adatom) O atoms, whose concentrations are denoted as α, β, and θ, respectively. O concentration in a given layer is defined as the ratio of the number of O atoms in that layer to the number of Ce atoms per trilayer. In the present study, α, β, and θ, were varied systematically and independently between 0 and 1 in increments of 0.25 (noting that an intact layer without vacancies contains 4 O atoms at the surface and sub-surface layers). This encompasses more than 20 configurations, ranging from an O depleted surface or sub-surface to a completely O adatom saturated surface.

We systematically start from a stoichiometric CeO_2 slab without any O adatoms ($\alpha = \beta = 1$, $\theta = 0$) and successively remove the surface or sub-surface O atoms from the 1st trilayer until the surface or sub-surface is devoid of O. These conformations simulate the surface transition of ceria as it undergoes reduction in a highly oxygen–lean/reducing environment. In addition to removing O atoms from the surface or sub-surface layers, several additional cases were considered in which surface and sub-surface O atoms were removed simultaneously. These included situations leading to a reduced Ce_2O_3 stoichiometry in the surface trilayer ($\alpha = \beta = 0.75$, $\theta = 0$), or to the surface trilayer completely devoid of O ($\alpha = \beta = \theta = 0$) which may occur under extremely reducing conditions. On the other hand, to model O adsorption on ceria in oxygen-rich/oxidizing conditions, θ was varied from 0 to 1 monolayers (ML) while maintaining the ceria stoichiometry ($\alpha = \beta = 1$). For a given concentration of the O adatom(s), three different adsorption sites, viz., top, bridge, and hollow (3-fold), were considered. To prevent ambiguity, we use the general notation $CeO_x^{\alpha,\beta} + \theta$ ML to represent the surface trilayer region including O adatoms. The trilayer stoichiometry is captured by x ($= \alpha + \beta$). For simplicity and to eliminate some redundancy, when $\theta = 0$, we represent the surface region by just $CeO_x^{\alpha,\beta}$; and when $\theta > 0$, we use the notation $CeO_2 + \theta$ ML (as $\alpha = \beta = 1$ when $\theta > 0$).

2.2. First principles thermodynamics

FPT has been extensively discussed in the past [37–39]; here we briefly remark on some key concepts only. The free energy for the formation of a certain concentration of O vacancies or adatoms $\left(G^f_{CeO_x^{\alpha,\beta}+\theta}\right)$ is defined as

$$G^f_{CeO_x^{\alpha,\beta}+\theta} = \frac{E_{CeO_x^{\alpha,\beta}+\theta} - E_{CeO_2} - 4(\alpha + \beta + \theta - 2)\mu_O}{|4(\alpha + \beta + \theta - 2)|}. \quad (1)$$

Here, $E_{CeO_x^{\alpha,\beta}+\theta}$ and E_{CeO_2} represent the 0 K DFT energy of the non-stoichiometric slab and the stoichiometric ceria slab ($\alpha = \beta = 1$, $\theta = 0$), respectively; and $4(\alpha + \beta + \theta - 2)$ represents the net number of O atoms that have been added to or removed from the stoichiometric slab (while noting that there are 4 O atoms per layer in the 2×2 (111) slab). μ_O is the oxygen chemical potential of the reservoir, which can be written in its temperature (T) and pressure (P) dependent form as

$$\mu_O\left(T, P_{O_2}\right) = \frac{1}{2}\left[E_{O_2} + \Delta\mu_{O_2}\left(T, P_{O_2}\right)\right], \quad (2)$$

where,

$$\Delta\mu_{O_2}\left(T, P_{O_2}\right) = \Delta\mu'_{O_2}(T, P^o) + kT \ln\left(\frac{P_{O_2}}{P^o}\right). \quad (3)$$

E_{O_2} in Eq. (2) represents the 0 K energy of an isolated O_2 molecule including the zero-point harmonic vibrational energy. $\Delta\mu_{O_2}$ contains the temperature and pressure dependent components, and can be separated into a purely temperature dependent part $\left(\Delta\mu'_{O_2}\right)$ that can be determined using the JANAF thermochemical tables [48] or statistical thermodynamics [49]. $kT \ln\left(\frac{P_{O_2}}{P^o}\right)$ accounts for the pressure dependence with a chosen reference pressure of P^o (1 atm). In deriving Eq. (1), the entropic and pressure–volume contributions to the free energy of condensed phases were neglected given that these effects would likely cancel out between the non-stoichiometric and stoichiometric slabs, as has been verified before by Zhu et al. [49].

Similarly, the surface energy corresponding to a slab with a certain concentration of O vacancies or adatoms, relative to the stoichiometric slab, is given by

$$\Delta\gamma_{CeO_x^{\alpha,\beta}+\theta} = \gamma_{CeO_x^{\alpha,\beta}+\theta} - \gamma_{CeO_2}$$
$$= \frac{E_{CeO_x^{\alpha,\beta}+\theta} - E_{CeO_2} - 4(\alpha + \beta + \theta - 2)\mu_O}{2\sigma}. \quad (4)$$

Here, $\Delta\gamma_{CeO_x^{\alpha,\beta}+\theta}$ is the relative surface energy; $\gamma_{CeO_x^{\alpha,\beta}+\theta}$ and γ_{CeO_2} are the surface energies of the non-stoichiometric and the stoichiometric slabs, respectively; and σ is the exposed surface area. The factor of 2 in the denominator accounts for the fact that our slab contains identical
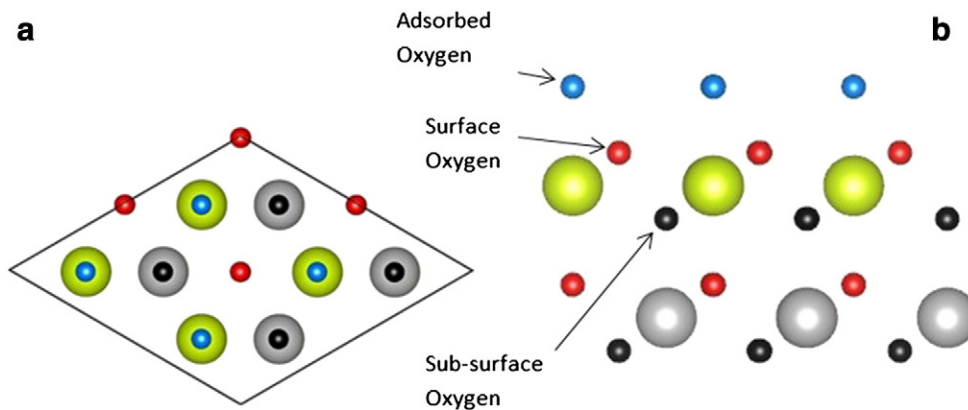

Fig. 3. (a) Top view of the ceria (111) 2×2 supercell, and (b) different O atoms in the slab model; red atoms — surface O, black atoms — sub-surface O, and blue atoms — adsorbed O. The green and gray atoms represent Ce in the 1st and 2nd trilayers, respectively.

top and bottom surfaces. The relative surface energy is used to identify the stable phases observed for a range of oxygen potentials. The driving force for O exchange is governed by the difference in the chemical potential between the solid and its environment. Low μ_O indicates an oxygen–lean environment in which O from the solid would likely desorb and create vacancies. Similarly, high μ_O indicates an oxygen-rich environment in which O adatoms would adsorb on the stoichiometric surface. Thus, μ_O is bound by two limits: a critical maximum when molecular O_2 condensation occurs on the surface and a critical minimum when μ_O is low enough to promote decomposition of ceria into its constituent components (Ce metal and O_2 gas).

The aforementioned equations apply to a ceria surface in equilibrium with an explicit O_2 reservoir. However, O transfer to and from the surface can also indirectly be facilitated by the presence of other redox environments (e.g., NO/NO_2, H_2/H_2O, and CO/CO_2). In such cases, μ_O is governed by the ratio of the gas concentrations or pressures, i.e., $\frac{P_{NO_2}}{P_{NO}}$, $\frac{P_{H_2O}}{P_{H_2}}$, or $\frac{P_{CO_2}}{P_{CO}}$, based on the following relations:

$$\mu_O = \mu_{NO_2} - \mu_{NO} \text{ or } \mu_O = \mu_{H_2O} - \mu_{H_2} \text{ or } \mu_O = \mu_{CO_2} - \mu_{CO}, \quad (5)$$

$$\mu_O\left(T, P_{NO_2}, P_{NO}\right) = \left[E_{NO_2} - E_{NO} + \Delta\mu'_{NO_2}(T, P^o) - \Delta\mu'_{NO}(T, P^o) + kT \ln\left(\frac{P_{NO_2}}{P_{NO}}\right) \right], \quad (6)$$

$$\mu_O\left(T, P_{H_2O}, P_{H_2}\right) = \left[E_{H_2O} - E_{H_2} + \Delta\mu'_{H_2O}(T, P^o) - \Delta\mu'_{H_2}(T, P^o) + kT \ln\left(\frac{P_{H_2O}}{P_{H_2}}\right) \right], \quad (7)$$

and

$$\mu_O\left(T, P_{CO_2}, P_{CO}\right) = \left[E_{CO_2} - E_{CO} + \Delta\mu'_{CO_2}(T, P^o) - \Delta\mu'_{CO}(T, P^o) + kT \ln\left(\frac{P_{CO_2}}{P_{CO}}\right) \right]. \quad (8)$$

Here, E_i represents 0 K energy, whereas the temperature dependent $\Delta\mu'_i$ terms for the different gases (i = NO, NO_2, H_2, H_2O, CO, CO_2) are obtained from the JANAF thermochemical tables [48]. The other terms are similar to those defined in Eqs. (2) and (3).

All the above mentioned relations apply to a thermodynamically governed system. Thus the stability of a surface is based on minimizing its free energy. The surface energy relation along with the expression for the oxygen potential allows for a one-to-one mapping between the stable surface phases and the operating variables (temperature and pressure), thereby allowing for the creation of the ceria surface phase diagram [37–39].

3. Results and discussion

3.1. 0 K energy of oxygen adatom(s) binding and vacancy formation

As alluded to earlier, the transition point when a surface readily switches between stoichiometric and non-stoichiometric states is particularly important in understanding the potential catalytic activity of

a particular material. In this section, in an attempt to understand such transitions, the dilute limit of O adatom binding or O vacancy formation in the stoichiometric ceria surface is explored. Table 1 shows the calculated 0 K formation energies for O adatoms on the surface, obtained by setting $\Delta\mu_{O_2}(T, P)$ to zero in Eq. (2). At $\theta = 0.25$ ML, which corresponds to a single O adatom on the 2×2 stoichiometric ceria slab, this simulates a dilute O adatom coverage on the ceria (111) surface. For this dilute coverage scenario, the binding energies with respect to molecular O_2 at the 3 different adsorption sites, viz., top, hollow, and bridge, are 2.24, 1.52, and 0.34 eV, respectively, at the PBE level of theory (the corresponding values are -1.08, -1.80 and -2.99 if the atomic O energy is used as a reference). Given that HSE06 is computationally expensive, we determined the adatom binding energy only for the stable bridge site, and obtained a similar binding energy value of 0.34 eV with respect to molecular O_2. Similarly, for PBE + U, the adatom binding energy for the stable bridge site was 0.38 eV with respect to molecular O_2. At the bridge site, the O–Ce bond length is 1.95 Å, whereas the bond length increases to 2.40 Å and 2.35 Å for the hollow and top sites, respectively. The short O–Ce bond length at the bridge site increases its bond strength, making it the most favorable site. Similarly at the hollow site, which is the second most stable site, the increased bond length reduces the orbital overlap thereby weakening its bond. However, at the hollow site, the O atom concurrently bonds with three neighboring Ce atoms, thus inducing greater stability relative to the top site binding. Furthermore, as the O adatom coverage increases from a dilute case ($\theta = 0.25$ ML) to one where the entire surface is covered with O adatoms ($\theta = 1$ ML), the bridge binding mode remains the most stable site followed by the hollow and top sites. Increasing the surface coverage of O adatoms results in larger adsorbate–adsorbate lateral repulsive interactions resulting in weaker O binding energies. These lateral interactions, however, are not significant even under high O coverage, given the large adatom separation in metal oxides compared to that in metals [50].

Having discussed the adatom cases, we now move to mildly reducing conditions where O vacancies start forming in the surface or sub-surface layers. Table 2 shows the 0 K energy required to form such an O vacancy, at the surface or sub-surface layer. In the dilute limit represented by a single vacancy in the 1st trilayer of the 2×2 slab, the energy required for an O vacancy formation at the surface or sub-surface layer is 3.27 and 2.98 eV, respectively. Therefore, a sub-surface O vacancy is more stable than a surface O vacancy by 0.29 eV. A similar DFT study comparing the relative stability of surface and sub-surface O vacancies in ceria indicates that a sub-surface vacancy is more stable than a surface vacancy by 0.29 eV due to lattice relaxations [30,51,52]. Nolan and colleagues also report a surface O vacancy formation energy of 3.30 eV [21,22]. The O vacancy formation calculations were repeated with the HSE06 level of theory, yielding a formation energy of 3.60 and 3.04 eV for a surface or sub-surface vacancy, respectively, in the 1st trilayer. We observed a slightly higher O surface vacancy formation energy compared to Pirovanno et al., mostly due to a lack of geometry optimization [30]. The corresponding values with PBE + U were 3.25 and 2.90 eV, respectively. In all three levels of theory, the sub-surface site is the more stable location for the point defect. The phenomenon of a more stable sub-surface vacancy has also been observed experimentally by Torbrugge and Reichling [16], where the nucleation of sub-surface vacancies occurs prior to the formation of surface vacancies

Table 1
Binding energy of O adatom(s) at different adsorption sites using molecular O_2 as reference. Values in parentheses are the binding energies with atomic O as the reference.

Coverage, θ ML	Top (PBE)	Hollow (PBE)	Bridge (PBE)	Bridge (PBE + U)	Bridge (HSE06)
0.25	2.24 (-1.08)	1.52 (-1.80)	0.34 (-2.99)	0.38 (-2.95)	0.34 (-2.25)
0.5a[a]	2.28 (-1.05)	1.58 (-1.75)	0.38 (-2.95)	0.34 (-2.99)	0.45 (-2.14)
0.5b[a]	2.28 (-1.05)	1.58 (-1.74)	0.42 (-2.91)	0.45 (-2.87)	0.48 (-2.11)
0.75	2.30 (-1.02)	2.19 (-1.14)	0.51 (-2.81)	0.65 (-2.68)	0.58 (-2.01)
1	2.32 (-1.02)	2.43 (-0.89)	0.58 (-2.74)	0.68 (-2.65)	0.69 (-1.91)

[a] (a) Vacancies or adatoms are adjacent to each other along the same axis; (b) vacancies or adatoms are not along the same axis in the 2×2 cell.

Table 2
Vacancy formation energies for a surface and sub-surface O in the 1st trilayer and at the upper and lower O layers of the 2nd and 3rd trilayers for a ceria (111) surface. The O vacancy formation energy in bulk CeO_2 is also shown for comparison.

Trilayer	Oxygen vacancy formation energy, eV					
	PBE		PBE + U		HSE06	
	Vacancy in upper layer	Vacancy in lower layer	Vacancy in upper layer	Vacancy in lower layer	Vacancy in upper layer	Vacancy in lower layer
1	3.27	2.98	3.25	2.90	3.60	3.04
2	3.97	3.91	–	–	–	–
3	3.85	3.85	–	–	–	–
Bulk	3.50		–		–	

as resolved via atomic and dynamic force microscopy. Table 2 reports the O vacancy formation energy for the 2nd and 3rd trilayers as well, using PBE. For the 2nd trilayer, creating an O vacancy requires 3.97 or 3.91 eV from an upper and lower O layer, respectively; whereas for the 3rd trilayer, 3.85 eV is required to remove an O from either of the O layers. Finally, we also report that the O vacancy formation energy for bulk CeO_2 is 3.50 eV, consistent with the value of 3.62 eV reported by Jiang et al. [27]. These results indicate that the bulk-like nature of the material is progressively recovered as one moves from the surface to the interior. It is also evident that removing O from the bulk-like internal trilayers requires significantly more energy and any underlying chemistry would likely be restricted to the surface (i.e., 1st trilayer). Therefore, we have considered O non-stoichiometry only at the 1st trilayer in the subsequent discussion.

3.2. Relative surface energies of configurations

Before incorporating the finite temperature and pressure effects, we look at the 0 K relative surface energy ($\Delta\gamma$) values for all the configurations considered (Table 3). The 0 K $\Delta\gamma$ values were computed by setting $\Delta\mu_{O_2} = 0$ in Eq. (2). Comparing cases with similar configuration from Table 3, i.e., as β (for $\alpha = 1$, $\theta = 0$) and α (for $\beta = 1$, $\theta = 0$) vary from 0 to 1, we observe that a reduced sub-surface is again preferred over a reduced surface, regardless of the O vacancy concentration. Along with the 0 K $\Delta\gamma$ values, Table 3 also compares the three levels of theory.

The agreement in $\Delta\gamma$ values among the three levels of theory is excellent, as indicated by the parity plot in Fig. 4 or by comparing the tabular values in Table 3. Validation of our calculated values with literature is challenging given that almost no information exists on non-stoichiometric ceria surfaces to the best of our knowledge. However, the ceria (111) surface energy value is widely reported, and thus we have used it as a basis of comparison. For a relaxed stoichiometric surface, past data range from 0.45 to 0.77 J/m^2 [18,19,27], which compare well with our calculated value of 0.56 J/m^2. The 0 K data provide a generic understanding of the surface; but the finite temperature and pressure contributions must be considered in real operating environments.

Next, we incorporate non-zero temperature and pressure effects using Eq. (3) into the relative surface energy relations in Eq. (4). Incorporating these factors results in a plot of $\Delta\gamma$ as a function of $\Delta\mu_{O_2}$ as shown in Fig. 5. As the relations mentioned in Section 2 are thermodynamically bound, the surface configuration with the lowest $\Delta\gamma$ is the most stable one. In Fig. 5, we observe that different surface configurations form the minimum trace line, as we progress gradually along the $\Delta\mu_{O_2}$ scale. The $\Delta\mu_{O_2}$ scale is indicative of the driving force for the exchange of O between the surface and its environment. At highly negative $\Delta\mu_{O_2}$ values, the environment is extremely reducing due to the lack of oxygen, which creates a systematic imbalance that forces O out from the slab. Under such conditions, a highly reduced surface with no surface or sub-surface O atoms is observed, i.e., the surface is Ce terminated. As $\Delta\mu_{O_2}$ becomes more positive, the imbalance created between the oxygen reservoir and the surface diminishes, thereby reducing the

Table 3
Relative surface energy, $\Delta\gamma$, for various O non-stoichiometry and adatom coverage configurations for ceria (111) at 0 K, with reference to the stoichiometric slab ($\alpha = \beta = 1$, $\theta = 0$). For non-zero adatom coverages ($\alpha = \beta = 1$, $\theta > 0$), the adatom location is also mentioned.

θ	α	β	$\Delta\gamma$, eV/Å^2		
			PBE	PBE + U	HSE06
0	1[a]	1[a]	0	0	0
0	1	0.75	0.058	0.058	0.059
		0.5a[b]	0.155	0.173	0.139
		0.5b[b]	0.142	0.148	0.139
		0.25	0.218	0.219	0.198
		0	0.321	0.310	0.278
	0.75	1	0.063	0.063	0.069
	0.5a[b]		0.188	0.208	0.173
	0.5b[b]		0.149	0.148	0.146
	0.25		0.269	0.297	0.239
	0		0.342	0.356	0.307
	0	0.75	0.450	0.460	0.419
		0.5a[b]	0.553	0.557	0.517
		0.5b[b]	0.862	0.831	0.869
		0.25	0.935	0.980	0.974
		0	0.786	0.778	0.739
	0.75	0.75c[c]	0.195	–	–
	0.75d[c]	0.75	0.150	–	–
0.25—top	1	1	0.043	–	–
0.25—hollow			0.029	–	–
0.25—bridge			0.007	0.011	0.007
0.5a[b]—top			0.088	–	–
0.5a[b]—hollow			0.061	–	–
0.5a[b]—bridge			0.015	0.019	0.017
0.5b[b]—top			0.088	–	–
0.5b[b]—hollow			0.061	–	–
0.5b[b]—bridge			0.016	0.022	0.018
0.75—top			0.133	–	–
0.75—hollow			0.086	–	–
0.75—bridge			0.030	0.038	0.034
1—top			0.179	–	–
1—hollow			0.188	–	–
1—bridge			0.045	0.052	0.058

[a] $\Delta\gamma = 0$ eV/Å^2 as CeO_2 is the reference. Calculated γ with PBE functional = 0.56 J/m^2.
[b] (a) Vacancies or adatoms are adjacent to each other along the same axis; (b) vacancies or adatoms are not along the same axis in the 2×2 cell.
[c] Vacancy at surface and sub-surface layer, with both the vacancies created by removing O atoms associated with a Ce atom or between a Ce atom and its nearest neighboring Ce atom, respectively.

extent of surface non-stoichiometry. Moving along the positive direction on the $\Delta\mu_{O_2}$ axis in Fig. 5, the heavily reduced Ce terminated surface configuration $CeO_0^{0,0}$ transitions to a $CeO_1^{1,0}$ configuration (sub-surface layer completely devoid of O), followed by a $CeO_{1.25}^{1,0.25}$ configuration
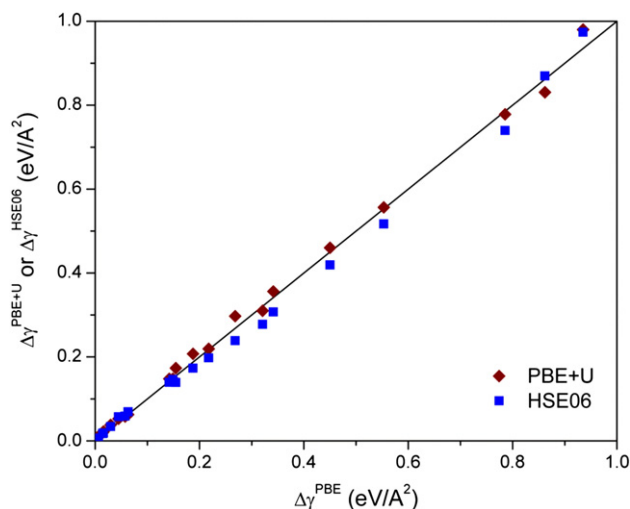

Fig. 4. Parity plot of PBE + U vs. PBE and HSE06 vs. PBE relative surface energy ($\Delta\gamma$) values for the configurations in Table 3.
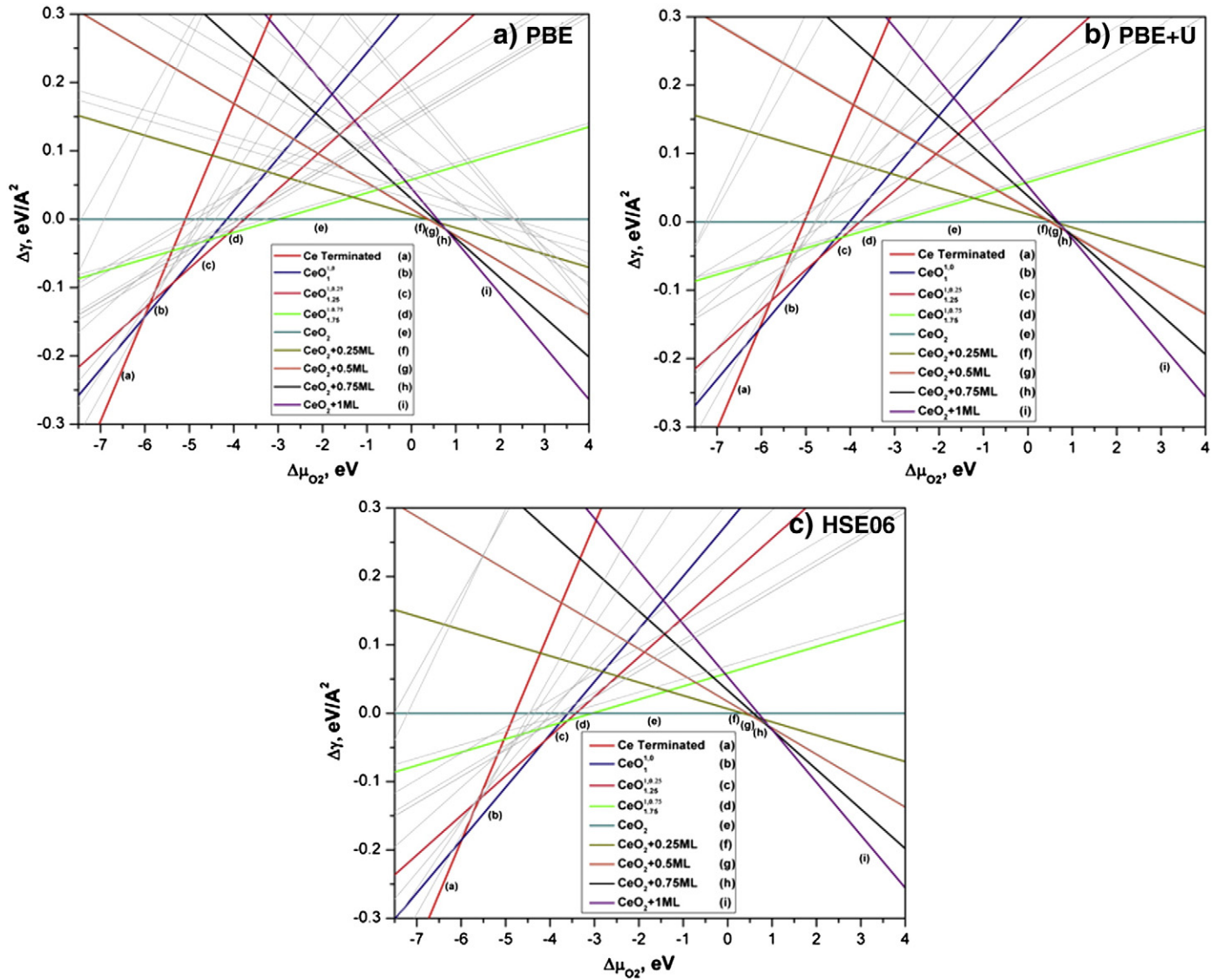
Fig. 5. Relative surface energy ($\Delta\gamma$) as a function of oxygen potential $\left(\Delta\mu_{O_2}\right)$ using the (a) PBE, (b) PBE + U, and (c) HSE06 functionals. Minimum energy line represents the most stable phases, whereas the intersection points depict phase transformation regions.

(sub-surface layer with high O vacancy concentration), followed by a marginally reduced $CeO_{1.75}^{1.0}$ configuration (sub-surface layer with low O vacancy concentration), and finally ending with a stoichiometric CeO_2 surface (no vacancies). With the current model, we do not observe the intermediate configuration of $CeO_{1.5}^{1.0}$. This particular stoichiometry is energetically unfavorable, and the stable phase switches between $CeO_{1.25}^{1.0}$ and $CeO_{1.75}^{1.0}$, as discussed in the sections to follow. At higher $\Delta\mu_{O_2}$ values (>0.35 eV for PBE, >0.4 eV for PBE + U, and >0.3 eV for HSE06), the onset for O adatom adsorption is observed on the ceria surface. These potentials represent an oxygen-rich environment, where a role reversal between the environment and the surface allows for adatom covered surfaces to be thermodynamically favorable. Starting from a stoichiometric or clean surface ($\theta = 0$), the O adatom coverage (θ) increases from 0 ML to 0.25 ML to 0.5 ML to 0.75 ML and finally to 1 ML (complete saturation) as the O_2 content in the environment increases.

At this point, we also note the similarities and differences among the PBE, PBE + U, and HSE06 derived $\Delta\gamma$ plots (Fig. 5a, b and c, respectively). In all the plots, the same stable phases are observed; the relative position of phase transformation however differs to some extent. Given that we solely optimized the electronic structure in HSE06 calculations, the configurations with significant rearrangement (primarily the heavily reduced

ones) show different oxygen potential locations for phase transition, and a geometric optimization could alter these boundaries. However, the initial reduction from CeO_2 to $CeO_{1.75}^{1.0}$ or the adatom adsorption from CeO_2 to CeO_2 + 0.25 ML occurs at similar $\Delta\mu_{O_2}$ conditions for all three levels of theory. Another key point, as described in Section 2, is that $\Delta\mu_{O_2}$ is bound by the two critical limits. In an oxygen–lean environment ($\Delta\mu_{O_2} < -5.23$ eV), the onset for the decomposition of the bulk material into its constituent elements, i.e., bulk Ce metal and O_2 gas, occurs. Using the stable phases and the critical conditions observed under different $\Delta\mu_{O_2}$ values allows us to create the ceria surface phase diagram under various oxygen environments.

3.3. First principles derived phase diagram for ceria

A mapping of the stable phases observed in Fig. 5 as a function of $\Delta\mu_{O_2}$ leads to the generation of the ceria surface phase diagram. Essentially, each $\Delta\mu_{O_2}$ value of Fig. 5, corresponding to a transition from one configuration to another, manifests as a curve in the phase diagram (as prescribed by Eq. (3)). Such a phase diagram is shown in Fig. 2 (PBE, PBE + U, and HSE06 results in panels a, b, and c, respectively). It reveals that under atmospheric pressure, a ceria surface remains in its

stoichiometric state even at extremely high temperatures (up to 2000 K). Progressing from the top left (close to ambient conditions) downwards (lower oxygen pressure) and to the right (higher temperatures), an imbalance between the O_2 reservoir and the surface causes O to desorb from ceria, making a mildly non-stoichiometric surface in the sub-surface layer to be the most stable phase. A further decrease in pressure (and oxygen potential) leads to a high degree of O desorption creating a more reduced sub-surface phase. Eventually under extremely high temperatures and low pressures (highly negative oxygen potentials), all the O atoms desorb from the sub-surface and surface layers, thereby creating a Ce terminated surface. All the manifestations observed in Fig. 5 are directly translated onto the ceria surface phase diagram in Fig. 2. The phases corresponding to adatom coverages do not appear under the conditions shown here, given that a practically unrealistic oxygen pressure is required ($P_{O_2} > 10^6$ atm) to observe any trace of adsorption.

After discussing the theoretical insights from the phase diagram, next we compare the phase diagram features with experimental data in literature. Symbols in Fig. 2 correspond to bulk ceria non-stoichiometry observed in an ensemble of experiments, such as thermo-gravimetric analysis, mass spectrometry, effusion measurements, high temperature X-ray diffraction, thermal expansion measurements, and specific heat measurements. The experimentally observed configurations include $CeO_{1.99}$, $CeO_{1.9}$, $CeO_{1.8}$, $CeO_{1.75}$, and $CeO_{1.7}$ [10,11]. The presence of ample experimental data allows for a direct comparison with the predicted non-stoichiometry. As seen in Fig. 2, the predicted phases are in good coherence with the experimental data. In order to observe any appreciable reduction of bulk ceria, ultra-low oxygen pressures and high temperatures are required, which is consistent with our predicted trend. As mentioned earlier, creating surface non-stoichiometry is energetically less taxing compared to bulk non-stoichiometry; therefore, surface reduction occurs prior to bulk reduction. This phenomenon is also captured by our phase diagram, which indicates the presence of a $CeO_{1.75}^{1.0.75}$ surface phase prior to the experimentally observed bulk stoichiometry of $CeO_{1.75}$. The dashed red line represents the thermodynamic conditions derived from DFT energies for bulk CeO_2 transitioning to its reduced Ce_2O_3 state. Again, in order to observe this transformation, the overall bulk stoichiometry must correspond to that of Ce_2O_3. The dashed purple line represents the thermodynamically governed conditions for the decomposition of bulk ceria into its constituent elements, i.e., Ce metal and O_2 gas. The difference observed in the position of the dashed lines between panels (a) and (b) lies in the governing theory used to create the thermodynamic transformations. For the HSE06 derived phases to be consistent, it is necessary to allow for structural relaxation. This may be important for only those cases where a significant rearrangement of the surface occurs as described earlier. On the other hand, for minimal rearrangement such as the initial transition of stoichiometric ceria to $CeO_{1.75}^{1.0.75}$, using the PBE + U or HSE06 theory results in only a marginal difference (the phase transformation occurs at a lower temperature by ~5 K with PBE + U and ~50 K with HSE06), indicating that the PBE level of theory is sufficient for practical purposes. Based on both theories, the region where ceria undergoes the initial phase transformation (transition of CeO_2 to $CeO_{1.75}^{1.0.75}$) is of utmost importance, as this governs the use of ceria as an O buffering material.

At this point, it is important to mention the limitations under which the phase diagram was derived: (i) The observed stable phases are limited by the initial domain of the configurations considered in this study. Additional intermediate configurations are therefore buried within the phase transition boundary, but they could be discerned using larger unit cell calculations. Nonetheless, the overall predictions based on the considered configurations are in excellent agreement with the experimental and thermodynamic data. (ii) The vibrational entropy contribution of the condensed phases to the total free energy is neglected. While this may be a good assumption at low temperatures (due to favorable cancelation of this contribution in the system before and after O adsorption/desorption) [49], this may have to be revisited at high temperatures close to the melting temperature. Given that the upper

temperature limit of the phase diagram is well below the melting point of the fluorite phase of ceria (~2650 K), we do not expect these effects to drastically alter the predicted energetics. (iii) The abrupt transitions in the derived stoichiometries will not be observed experimentally, but they are rather a manifestation of ignoring the configurational entropy (and point (i) made above). (iv) The dynamics of vacancy filling and migration are not considered here. (v) Using a PBE based geometry as a baseline can induce the formation of Ce^{3+} ions more readily. (vi) Lastly, using a PBE functional results in a delocalization of electrons (charge density plots showing the extent of delocalization between the two functionals are provided in the supplementary information), but captures the initial phase transformation accurately given that energetics is not significantly altered under a dilute vacancy limit. Despite these assumptions and limitations, we expect the predictions made using such strategies to be at least semi-quantitative in systems involving O chemistry, as has been pointed out earlier [49], and as is clearly borne out by the current work. The predicted phases not only validate experimentally observed transitions, but are also in excellent agreement with the experimental and thermodynamic data.

3.4. Bader analysis to determine the oxidation states

To further validate the stable phases predicted by FPT calculations, we performed a Bader analysis to determine the oxidation states of the Ce atoms under different O environments. Ce atoms in CeO_2 and Ce_2O_3 have a formal oxidation state of +4 and +3, respectively. However, the nominal oxidation states as recovered by the Bader analysis are expected to be different from these formal values due to incomplete charge transfer and the inability to unambiguously partition space in order to determine the formal atomic charge. In our calculations, bulk ceria in a nominal +4 and +3 state exhibits a Bader oxidation state of +2.23 and +1.98, respectively. These oxidation states are similar to the bulk values (+2.37 and +1.98) reported by Loschen et al. [51]. Using these values as a benchmark, we compared the oxidation states of Ce atoms in each trilayer for all the configurations to distinguish whether the Ce atom is in an oxidized (+4) or reduced (+3) state. Fig. 6 shows the Bader charge of the Ce atoms as we progress from the 1st trilayer down to the bulk-like internal trilayers. The two dotted lines in Fig. 6 represent the Bader oxidation states of the Ce atoms in bulk CeO_2 and Ce_2O_3. The $CeO_{1.75}^{1.0.75}$ configuration has an oxidation state (+2.37) similar to bulk CeO_2, whereas the $CeO_{1.25}^{1.0.25}$ configuration has an oxidation state (+1.98) similar to bulk Ce_2O_3. This indicates why the intermediate $CeO_{1.5}^{1.0.5}$ configuration does not show up as a stable phase in the relative surface energy plot. For any intermediate oxidation states, this configuration is not energetically favored. A similar reduction
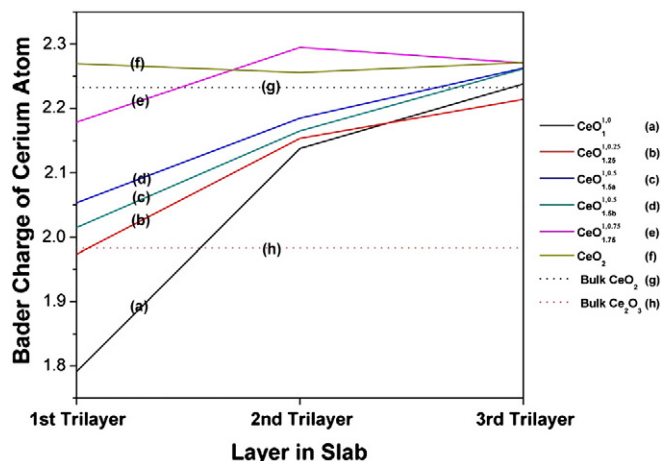

Fig. 6. Bader charge distribution of Ce atoms progressing from the 1st trilayer at the surface to the internal bulk-like 3rd trilayer.

in the Bader charge (~0.1 eV) on progressing to non-stoichiometric cases has been reported with ceria nanoparticles whereby the reduced co-ordination affects bonding between the Ce and O ions, and also affecting the surface energy as a result [53]. Finally, as we move into the material (i.e., the inner trilayers), the Bader oxidation state of bulk CeO_2 is recovered; and thus the energy required for forming an O vacancy from the 2nd and 3rd trilayers is equivalent to that of an O vacancy from bulk CeO_2. This is also consistent with the conclusion drawn from the O vacancy formation energy.

3.5. Ceria phase diagram with indirect oxygen participation

As discussed earlier, in the presence of a reducing/oxidizing environment, O transfer can occur via an indirect redox reaction of ceria with various gas molecule pairs. FPT serves as a powerful tool to consider these situations of indirect O participation, as discussed in Section 2 and Eqs. (6)–(8). Given that the relative difference in surface stoichiometry changes marginally when using PBE + U or HSE06, we re-derived the ceria surface phase diagrams in three equilibrium redox environments – NO/NO_2, H_2/H_2O, and CO/CO_2 – (Fig. 7a, b, and c, respectively) using PBE energetics. The critical assumptions made while deriving these phase diagrams are as follows: (i) Direct interactions of CO, CO_2, H, H_2O, NO, and NO_2 with the ceria surface are not included, i.e., the energetics of adsorption and surface reactions involving these species are not incorporated. (ii) The oxygen potential is defined based on a single redox reaction given in Section 2, whereas several side reactions could be possible in a real environment.

The phase diagrams in Fig. 7 were derived in terms of the ratio of the partial pressures, which governs the oxygen chemical potential as discussed earlier. A low ratio indicates an oxygen deficient (reducing) environment. Fig. 7a, b, and c indicate that the ceria surface is readily reduced in the CO-rich and H_2-rich environments [54,55], as compared to an NO-rich environment which requires higher temperatures for the

same extent of non-stoichiometry. This is consistent with the notion that H_2 and CO are stronger reducing gases compared to NO [50]. Given assumptions (i) and (ii) above, the difference in the predicted phases in H_2/H_2O and CO/CO_2 environments (Fig. 7b and c) is a direct manifestation of the thermodynamics governing their corresponding oxidation reactions. For any given temperature, a decrease in the ratio of partial pressures lowers the oxygen potential, therefore creating a reduced surface. The extent of non-stoichiometry increases as the temperature increases or the ratio of partial pressures decreases. Once again, the predicted phases are in good agreement with the experimentally observed phases of ceria under the considered redox environments [10].

3.6. Implications of O vacancy formation energy for catalysis and materials design

The work presented thus far demonstrates our ability to make the high-fidelity predictions of phase transitions enabled by chemical processes on ceria surfaces using DFT–FPT. In order to use this scheme to tailor the activity of ceria for redox catalysis, e.g., through doping, it may be useful to identify the most important factor (or the "descriptor") that controls the surface oxygen chemistry of ceria [56]. Based on our results, we believe that the O vacancy formation energy is such a descriptor as it largely governs the transition of stoichiometric ceria to a reduced phase, where active sites are created. Indeed, factors that control the placement of relevant phase boundaries have been shown in the past to correlate to catalytic activity [57,58]. Moreover in this work, even though the sub-surface O vacancy formation energy is identified as a descriptor, both the surface and sub-surface vacancies could play an active role after equilibration. Based on the experimental work by Torbrugge et al. [16] and Esch et al. [28], both types of vacancies exist at ~1300 K, and the active rearrangement of the vacancies indicates the availability of defect sites for reactions (outside the scope of our work). O vacancies on a ceria surface also drive water dissociation into OH and H – a
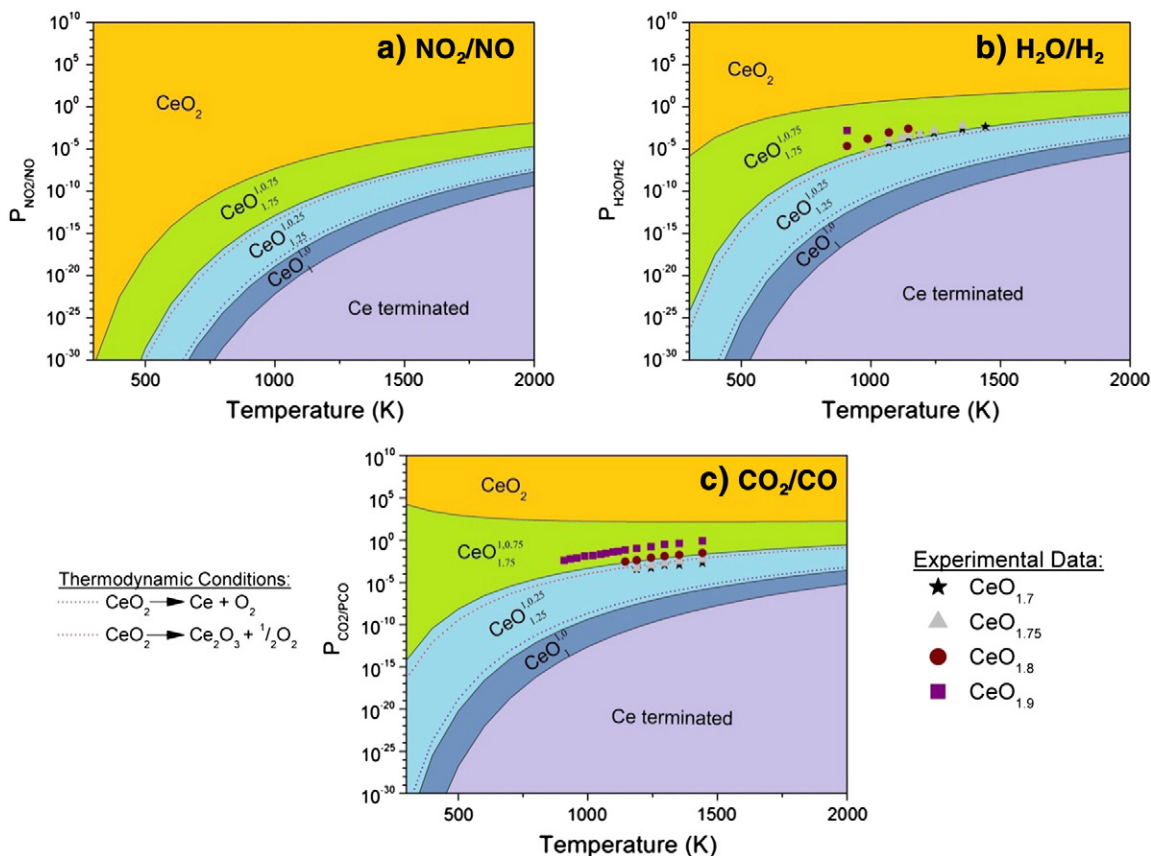

Fig. 7. Ceria surface phase diagram derived in (a) NO/NO₂, (b) H₂/H₂O, and (c) CO/CO₂ redox environments using the PBE functional. Symbols represent experimental data [10].

pre-requisite for WGS reaction [59,60] – as shown by Fronzi et al. [32]. O vacancies on a ceria surface are known to be thermodynamically favorable during CO oxidation — another key component of the WGS reaction [61]. The creation of such vacancies in a CO environment could provide nucleation sites for water dissociation, which could explain the improved performance of ceria in WGS [4,5,7,9]. Recently, Janik and colleagues reported the role of O vacancies (ceria surface reduction) and metal doping in hydrocarbon conversion [31]. The O vacancies were shown to directly lower the dissociation energy of methane on a reduced surface. The collective evidence signifies the crucial role of O vacancies in chemical reactions involving ceria. As these vacancies play a key role in promoting surface reactions, measuring them and understanding their properties are critical in explaining the trends among new catalytic materials being developed or synthesized. Having identified the O vacancy formation energy as the *descriptor*, a framework for the predictive design of novel ceria-based materials for catalytic processes involving oxygen chemistry can be established.

4. Conclusions

In this work, we have derived the first ceria (111) surface phase diagram in four types of oxygen environments involving direct and indirect oxygen participation using first principles thermodynamics. Our results correlate well with literature experimental data in every case where such comparisons can be made. A stoichiometric ceria surface in a pure O_2 environment is highly stable; and any appreciable surface reduction occurs only under extreme temperatures and oxygen pressures. Surface reduction is however more facile in the presence of a redox environment (NO/NO_2, H_2/H_2O, or CO/CO_2). H_2 and CO, being strong reducing agents, promote O capture from the sub-surface at any given temperature, as compared to an NO or a pure O_2 environment. Transition from a stoichiometric to a reduced surface is a crucial factor in governing the surface reactivity of ceria in redox reactions. Irrespective of the level of theory used here (involving semi-local, modified semi-local, and hybrid electronic exchange correlation functionals), this transition occurs at similar temperature and pressure conditions. The O vacancy formation energy primarily drives this transition and can thus be viewed as a *descriptor* for the catalytic activity of ceria in redox reactions. The predictive power of the first principle thermodynamics approach for describing the surface oxygen chemistry of ceria immediately opens up the possibility for further optimization of this system via descriptor-driven materials design.

Acknowledgments

References

[1] A. Trovarelli, Catalysis by Ceria and Related Material, 1, 2002. (508-3-15).
[2] Y. Liu, Y. Ding, L. Zhang, Y. Lei, RSC Adv. 2 (2012) 5193.
[3] W.C. Chueh, S. Haile, Philos. Trans. A Math. Phys. Eng. Sci. 368 (2010) 3269.
[4] S. Hilaire, A. Wang, T. Luo, R.J. Gorte, J. Wagner, Appl. Catal. A Gen. 215 (2001) 271.
[5] G. Jacobs, E. Chenu, P.M. Patterson, L. Williams, D. Sparks, G. Thomas, B.H. Davis, Appl. Catal. A Gen. 258 (2004) 203.
[6] J. Kugai, J.T. Miller, N. Guo, C. Song, Appl. Catal. B Environ. 105 (2011) 306.
[7] C. Wheeler, A. Jhalani, E.J. Klein, S. Tummala, L.D. Schmidt, J. Catal. 223 (2004) 191.
[8] R.J. Gorte, AIChE J 56 (2010) 1126.
[9] R.J. Gorte, S. Zhao, Catal. Today 104 (2005) 18.
[10] D.J.M. Bevan, J. Kordis, J. Inorg. Nucl. Chem. 26 (1964) 1509.
[11] R.J. Panlener, R.N. Blumenthal, J.E. Garnier, J. Phys. Chem. Solids 36 (1975) 1213.
[12] R.J. Ackermann, E.G. Rauh, J. Chem. Thermodyn. 3 (1971) 609.
[13] R.G. Schwab, R.A. Steiner, G. Mages, H.J. Beie, Thin Film Solids 207 (1992) 288.
[14] R. Körner, M. Ricken, J. Nölting, I. Riess, J. Solid State Chem. 78 (1989) 136.
[15] M. Ricken, J. Nolting, J. Solid State Chem. 54 (1984) 89.
[16] S. Torbrugge, M. Reichling, Phys. Rev. Lett. 99 (2007) 1.
[17] J.L.F. Da Silva, M.V.G. Pirovano, J. Sauer, V. Bayer, G. Kresse, Phys. Rev. B 75 (2007) 1.
[18] M. Fronzi, A. Soon, B. Delley, E. Traversa, C. Stampfl, J. Chem. Phys. 131 (2009) 1.
[19] T. Desaunay, A. Ringuede, M. Cassir, F. Labat, C. Adamo, Surf. Sci. 606 (2012) 305.
[20] C.W. Castleton, J. Kullgren, K. Hermansson, J. Chem. Phys. 157 (2007) 1.
[21] M. Nolan, S. Parker, G.W. Watson, Surf. Sci. 595 (2005) 223.
[22] M. Nolan, J.E. Fearon, G.W. Watson, Solid State Ionics 177 (2006) 3069.
[23] P.P. Dholabhai, J.B. Adams, P. Crozier, R. Sharma, J. Chem. Phys. 132 (2010) 1.
[24] M.M. Branda, R.M. Ferullo, M. Causa, F. Illas, J. Phys. Chem. C 115 (2011) 3716.
[25] Z. Yang, T.K. Woo, K. Hermansson, J. Chem. Phys. 120 (2004) 1.
[26] S. Shi, Y. Tang, C. Ouyang, L. Cui, X. Xin, P. Li, W. Zhou, H. Zhang, M. Lei, L. Chen, J. Phys. Chem. Solids 71 (2010) 788.
[27] Y. Jiang, J.B. Adams, M.V. Schilfgaarde, J. Chem. Phys. 123 (2005) 1.
[28] F. Esch, S. Fabris, L. Zhou, T. Montini, C. Africh, P. Fornasiero, G. Comelli, R. Rosei, Science 309 (2005) 752.
[29] C.T. Campbell, C.F. Peden, Science 309 (2005) 713.
[30] M.V.G. Pirovano, J.L.F. Da Silva, J. Sauer, Phys. Rev. Lett. 102 (2009) 1.
[31] M.D. Krcha, A.D. Mayernick, M.J. Janik, J. Catal. 293 (2012) 103.
[32] M. Fronzi, S. Piccinin, B. Delley, E. Traversa, C. Stampfl, Phys. Chem. Chem. Phys. 11 (2009) 9188.
[33] C. Zhang, A. Michaelides, D.A. King, S.J. Jenkins, Phys. Rev. B 79 (2009) 1.
[34] H.Y. Li, H.F. Wang, X.Q. Gong, Y.L. Guo, Y. Guo, G. Lu, P. Hu, Phys. Rev. B 79 (2009) 1.
[35] C. Loschen, J. Carrasco, K.M. Neyman, F. Illas, Phys. Rev. B 75 (2007) 1.
[36] S. Fabris, S. Gironcoli, S. Baroni, G. Vicario, G. Balducci, Phys. Rev. B 71 (2005) 1.
[37] K. Reuter, D. Frenkel, M. Scheffler, Phys. Rev. Lett. 93 (2004) 1.
[38] K. Reuter, M. Scheffler, Phys. Rev. Lett. 90 (2003) 1.
[39] J. Roga, K. Reuter, M. Scheffler, Phys. Rev. Lett. 98 (2007) 1.
[40] G. Kresse, J. Furthmuller, Phys. Rev. B 54 (1996) 169.
[41] P.E. Blochl, Phys. Rev. B 50 (1994) 953.
[42] G. Kresse, D. Joubert, Phys. Rev. B 59 (1999) 1758.
[43] J.P. Perdew, K. Burke, Y. Wang, Phys. Rev. B 54 (1996) 533.
[44] J. Heyd, G.E. Scuseria, M. Ernzerhof, J. Chem. Phys. 118 (2003) 8207.
[45] J.F. Herbst, R.E. Watson, J.W. Wilkins, Phys. Rev. B 17 (1978) 3089.
[46] V.I. Anisimov, O. Gunnarsson, Phys. Rev. B 43 (1991) 7570.
[47] L. Gerward, J.S. Olsen, L. Petit, G. Vaitheeswaran, V. Kanchana, A. Svane, J. Alloys Compd. 400 (2005) 56.
[48] D.R. Hull, H. Prophet, JANAF Thermochemical Tables 37 (1971).
[49] H. Zhu, C. Tang, R. Ramprasad, Phys. Rev. B 82 (2010) 1.
[50] R. Getman, Y. Xu, W. Schneider, J. Phys. Chem. C 112 (2008) 9559.
[51] C. Loschen, A. Migani, S.T. Bromley, F. Illas, K.M. Neyman, Phys. Chem. Chem. Phys. 10 (2008) 5730.
[52] M.V. Ganduglia-Pirovano, A. Hofmann, J. Sauer, Surf. Sci. Rep. 62 (2007) 219, http://dx.doi.org/10.1016/j.surfrep.2007.03.002.
[53] N. Nilius, S.M. Kozlov, J.F. Jerratsch, M. Baron, X. Shao, F. Vines, S. Shaikhutdinov, K.M. Neyman, H.J. Freund, ACS Nano 6 (2012) 1126, http://dx.doi.org/10.1021/nn2036472.
[54] A. Bueno-Lopez, K. Krishna, M. Makkee, J.A. Moulijn, Catal. Lett. 99 (2005) 203, http://dx.doi.org/10.1007/s10562-005-2120-x.
[55] M.A. Henderson, C.L. Perkins, M.H. Engelhard, S. Thevuthasan, C.H.F. Peden, Surf. Sci. 526 (2003) 1, http://dx.doi.org/10.1016/S0039-6028(02)02657-2.
[56] J.K. Norskov, T. Bligaard, J. Rossmeisl, C.H. Christensen, Nat. Chem. 1 (2009) 37.
[57] K. Reuter, M. Scheffler, Phys. Rev. B 73 (2006) 045433.
[58] G. Pilania, P.X. Gao, R. Ramprasad, J. Phys. Chem. C 116 (2012) 26349.
[59] A.B. Mhadeshwar, D.G. Vlachos, J. Catal. 234 (2005) 48.
[60] A.B. Mhadeshwar, D.G. Vlachos, J. Phys. Chem. B 108 (2004) 15246.
[61] T.X.T. Sayle, S.C. Parker, C.R.A. Catlow, Surf. Sci. 316 (1994) 329.